Inversion of Wave Parameters With Shore-Based Coherent S-Band Radar Using Quasi-Binary Variational Mode Decomposition

Zhongqian Hu [ID], Zezong Chen [ID], Chen Zhao [ID], *Member, IEEE*, and Xi Chen [ID]

Abstract—Coherent microwave radar utilizes the direct relationship between the orbital wave velocity and the wave height spectrum to retrieve wave parameters. However, due to the broken wave and its evolution, "Group-Line" is introduced in the radar-obtained wavenumber–frequency spectrum, and the dominant wave energy is reduced. Many methods have proposed to remove "Group-Line" in the wavenumber–frequency spectrum, but these methods can only remove low-frequency energy and fail to compensate for the dominant wave energy. To solve this problem, a method for wave parameter inversion using quasi-binary variational mode decomposition (QB-VMD) is proposed. First, QB-VMD decomposes the spatial–temporal radial velocity series, and a series of modes is obtained, including "Group-Line" and dominant wave modes. Second, the "Group-Line" mode is discarded, and the dominant wave mode is compensated appropriately to reconstruct the spatial–temporal radial velocity series. Finally, the wave parameters are retrieved according to the reconstructed spatial–temporal radial velocity series. The proposed method is verified by simulation. In addition, this article uses an eight-day dataset collected by the coherent S-band radar deployed at Beishuang island for analysis. The significant wave height and mean wave period are retrieved from the dataset. The wave parameters estimated by the proposed method are compared with the buoy results. The correlation coefficients are 0.97 and 0.80, and the root-mean-square errors are 0.12 m and 0.49 s, respectively. The results show that the proposed method can invert wave parameters using the coherent S-band radar with reasonable performance.

Index Terms—Broken waves, coherent S-band radar, quasi-binary variational mode decomposition (QB-VMD), wavenumber–frequency spectrum, wave parameter inversion.

I. INTRODUCTION

WAVE observation plays an important role in ocean engineering, offshore operations, and marine environmental

monitoring. In situ measurements, such as wave buoys [1], are usually regarded as "sea-truth"[2]. With the development of remote sensing technology, radar and other remote sensing devices are widely used in the field of marine monitoring taking advantage of all-weather real-time performance and relatively low cost [3], [4]. As a remote sensing device with high spatial–temporal resolution [5], coherent and noncoherent microwave radar retrieves wave information based on the Bragg scattering between electromagnetic waves and gravity-capillary waves on the sea surface [6], [7].

Since the signals emitted by coherent microwave radar have all determined phase angles, this feature provides the ability to obtain the radial Doppler velocity of the water particle [2], [8], [9], [10], [11]. The direct relationship between the radial velocity and the wave height spectrum can be used to retrieve ocean wave parameters such as significant wave height (H_s) and mean wave period (T_{av}) [12], [13]. The characteristics of high spatial–temporal resolution enable coherent microwave radar to detect nonlinear details in the sea surface, such as broken waves [14]. Stevens et al. [15] analyzed the energy distribution characteristics in the wavenumber–frequency spectrum. Subsequently, Plant and Farquharson [16] used an X-band microwave radar to study that broken waves would cause nonlinear features such as "Group-Line" in the wavenumber–frequency spectrum. Due to the existence of these nonlinear characteristics, additional components will be generated in the low frequency of the radar-estimated wave spectrum, and the dominant wave energy will be reduced [17], [18], which leads to the overestimation of wave parameters, especially the mean wave period [13], [17]. Therefore, many studies focus on removing the nonlinear components from the wavenumber–frequency spectrum to improve the accuracy of ocean wave parameter inversion. Kammerer and Hackett [19], [20], [21] demonstrated that retaining part of "Group-Line" energy in significant wave height inversion can improve inversion accuracy when "Group-Line" energy is greater than or comparable with dispersion curve energy. Hwang et al. [22] used a high-pass filter with a cutoff frequency of 0.04 Hz to filter out part of "Group-Line" energy, but the wave period was overestimated. Chen et al. [8] set the cutoff frequency to 0.05 Hz and obtained a good wave height result, but the wave period was still overestimated. Different from this method of retaining part of "Group-Line," Carrasco et al. [23] filtered out all the "Group-Line" and high-order harmonic components and

only kept the dominant wave energy on the dispersion relation. However, the wave period was still overestimated. Subsequently, Liu et al. [18] proposed a microwave composite scattering model on the sea surface considering broken wave and its evolution, which explained the generation mechanism of "Group-Line" in the wavenumber–frequency spectrum and provided a theoretical basis for improving the wave measurement performance of coherent microwave radar. Based on this model, Chen et al. used a high-pass filter [2] and a dispersion relation filter [17] to obtain relatively accurate significant wave height and mean wave period parameters, respectively. Recently, He et al. [12] have proposed a spectral proper orthogonal decomposition method, which removes the nonwave contribution and improves the inversion results of ocean wave parameters. Unlike the spatial–temporal dimension approach, Zhao et al. [13] have recently proposed a method to retrieve ocean wave parameters only from the time Doppler spectrum collected with the coherent *S*-band radar, which can retrieve ocean wave parameters without spatial observations. Yang and Huang [24] obtained ten intrinsic mode functions (IMFs) by variational mode decomposition (VMD) of *X*-band radar subimages and obtained reasonable wave height by linear fitting using the sum of amplitude modulation components extracted from the sixth to the ninth IMF components, but did not verify the wave period parameters.

However, it is difficult for the above methods to simultaneously estimate accurately significant wave height and mean wave period. In order to solve this problem, a method based on quasibinary variational mode decomposition (QB-VMD) is proposed to retrieve ocean wave parameters in the article. QB-VMD is a 2-D form of VMD, which has been proposed to solve the identification and separation of multiscale coherent structures in scale interactions in wall turbulence [25], [26]. Wang et al. [25] showed that QB-VMD has the advantages of scale representation and energy reconstruction. In this article, QB-VMD is used to decompose the spatial–temporal radial velocity series to obtain a series of modes. Then, the "Group-Line" modes are removed, and the dominant wave modes are appropriately compensated to obtain the reconstructed spatial–temporal radial velocity series. Finally, the wave height spectrum is estimated from the reconstructed spatial–temporal radial velocity series, and the ocean wave parameters are retrieved. The inversion algorithm is verified using an eight-day dataset collected with a coherent *S*-band radar MORSE deployed at Beishuang island.

The rest of this article is organized as follows. Section II introduces the principle of radar wave measurement and the impact of broken wave and also describes the proposed method and the inversion process of wave parameters in detail. Section III validates the proposed method through simulations. Section IV analyzes the measured data over eight days to evaluate the algorithm performance and discusses the results. Finally, Section V concludes this article.

II. WAVE MEASUREMENT PRINCIPLE AND METHOD

A. Principle of Radar Wave Measurement

As shown in Fig. 1, when the radar irradiates the sea surface at an incident angle θ, the radial orbital velocity of the water
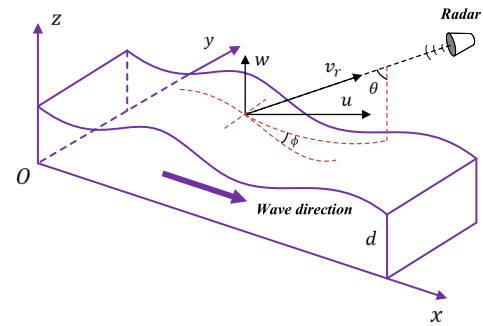

Fig. 1. Schematic diagram of surface wave velocity measured by radar.

particles on the sea surface is

$$v_r(x,t) = u(x,t)\sin(\theta) + w(x,t)\cos(\theta) \qquad (1)$$

where x is the distance, t is the time, and u and w are the horizontal and vertical components of orbital speed, respectively, which can be represented as [27]

$$u(x,t) = A\omega \coth(kd)\cos(kx \pm \omega t)\cos(\phi) \qquad (2)$$

$$w(x,t) = A\omega \sin(kx \pm \omega t) \qquad (3)$$

where A is the amplitude, k is the wavenumber, d is the water depth, and ϕ denotes the angle between the radar illumination direction and the wave propagation direction. Under the condition of deep water in the absence of sea surface current, the angular frequency and the wavenumber satisfy the dispersion relation $\omega^2 = \pm gk$, where g is the acceleration of gravity. The positive (negative) sign indicates approaching (moving away from) the radar. The 1-D radial velocity spectrum of a single traveling wave can be obtained via the fast Fourier transform (FFT) at the range cell x_0 using (1)

$$V(f) = \frac{\omega A(f)}{\tanh(kd)} \cdot \frac{M}{2} \cdot [\sin(\theta) - j \cdot \cos(\theta)\tanh(kd)] \quad (4)$$

where M is the number of time sampling points and f is the wave frequency. According to the relationship between the wave amplitude and the wave spectrum, we have

$$\frac{1}{2}A^2(f) = S(f,\varphi) \cdot \Delta f \cdot \Delta\varphi \qquad (5)$$

where $S(f,\varphi)$ denotes the radial wave spectrum, Δf is the frequency resolution, φ is the radar antenna observation direction, and $\Delta\varphi$ is the angle resolution. Therefore, the transfer function between the 1-D radial velocity power spectrum and the wave spectrum can be expressed as

$$TF = \frac{2\tanh^2(kd)}{\omega^2 M^2 \Delta f \Delta\varphi(\sin^2(\theta) + \cos^2(\theta)\tanh^2(kd))}. \qquad (6)$$

B. Impact of Broken Waves

The composite surface model divides the ocean surface into long gravity waves, intermediate-scale waves, and small-scale waves. The small-scale waves are tilt-modulated and advected by the long gravity wave [6], [28]. Usually, small-scale waves have small slopes and displacements and propagate freely at
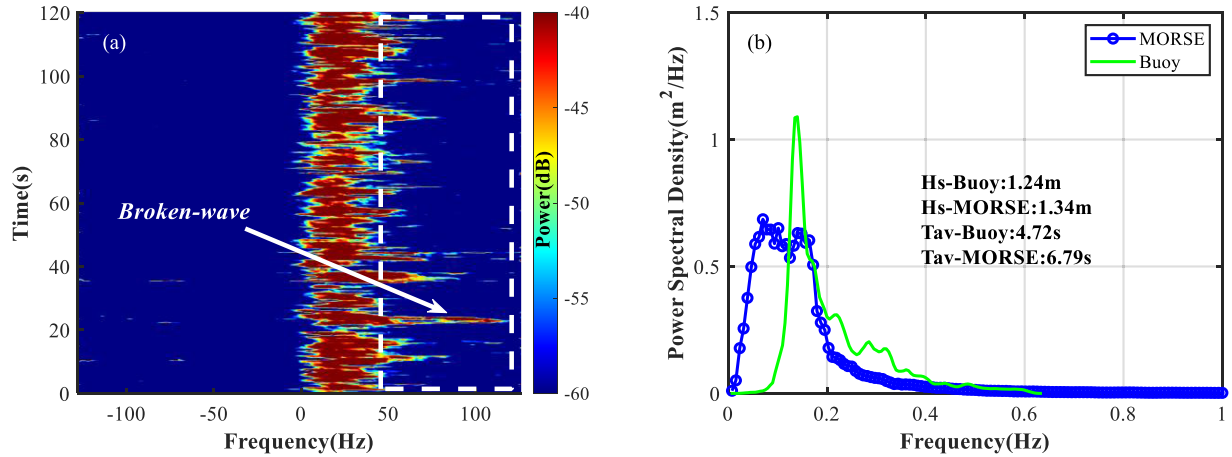
Fig. 2. MORSE measured echoes from 12:05 to 12:23 on March 22, 2015. (a) Time–Doppler spectrum at the 58th range cell for the fourth antenna. (b) Nondirectional wave height spectrum. "Buoy" and "MORSE" represent buoy and radar, respectively.
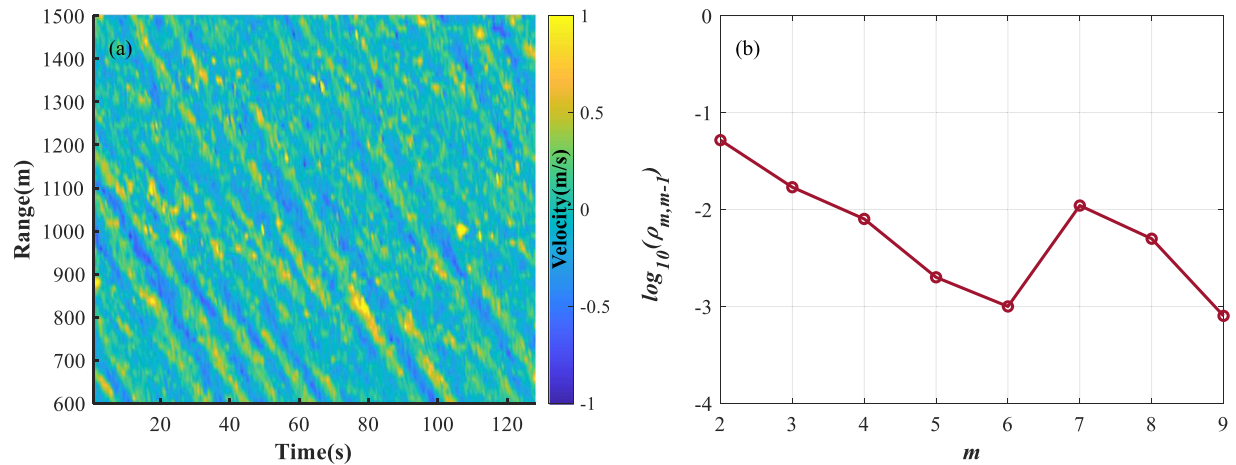

Fig. 3. Spatial–temporal velocity series and the corresponding $\rho_{m,m-1}$. (a) Spatial–temporal velocity series. (b) $\rho_{m,m-1}$ against m value of (a).

their phase velocity, also called free waves. In deep water, due to the modulation of long gravity waves, intermediate-scale waves become steep enough at a phase of the dominant wave to break up [29]. The broken waves begin to propagate at the phase velocity of the intermediate-scale waves and gradually decrease to the phase velocity of the free waves with time [30]. The electromagnetic waves transmitted by the coherent S-band radar generate Bragg scattering not only with the free wave but also with the broken waves.

Fig. 2 shows an example of the echoes collected with the MORSE at Zhelang island from 12:05 to 12:23 on March 22, 2015. In Fig. 2(a), the white arrow indicates the "spike" phenomenon in the Doppler spectrum caused by the broken waves [13], [18]. It can be seen from the white dotted box that the broken waves cause the sea echoes to broaden to the right intermittently. The Doppler frequency shift f_d can be calculated according to the spectral moment method

$$f_d = \frac{\int f\sigma(f)df}{\int \sigma(f)df} \tag{7}$$

where f_d is the Doppler frequency and $\sigma(f)$ is the Doppler spectrum. Then, the radial velocity can be expressed as

$$v_r = \frac{f_d \cdot \lambda_0}{2} \tag{8}$$

where λ_0 is the radar electromagnetic wave wavelength. Equation (8) shows that the radial velocity would suddenly change due to the intermittent broadening of the Doppler spectrum, which leads to a change in the retrieved wave height spectra. Fig. 2(b) shows the comparison between the wave height spectra obtained by the MORSE and the buoy during this period. In the MORSE-estimated wave height spectrum, the additional power at low frequencies is generated, and the dominant wave power decreases. The significant wave height is basically consistent with the buoy, while the mean wave period is overestimated.

C. Quasi-Binary Variational Mode Decomposition

QB-VMD treats the 2-D radial velocity $v_r(x,t)$ as a collection of slices along the primary direction (t direction herein) with distinct scale separation. In addition, the continuity of
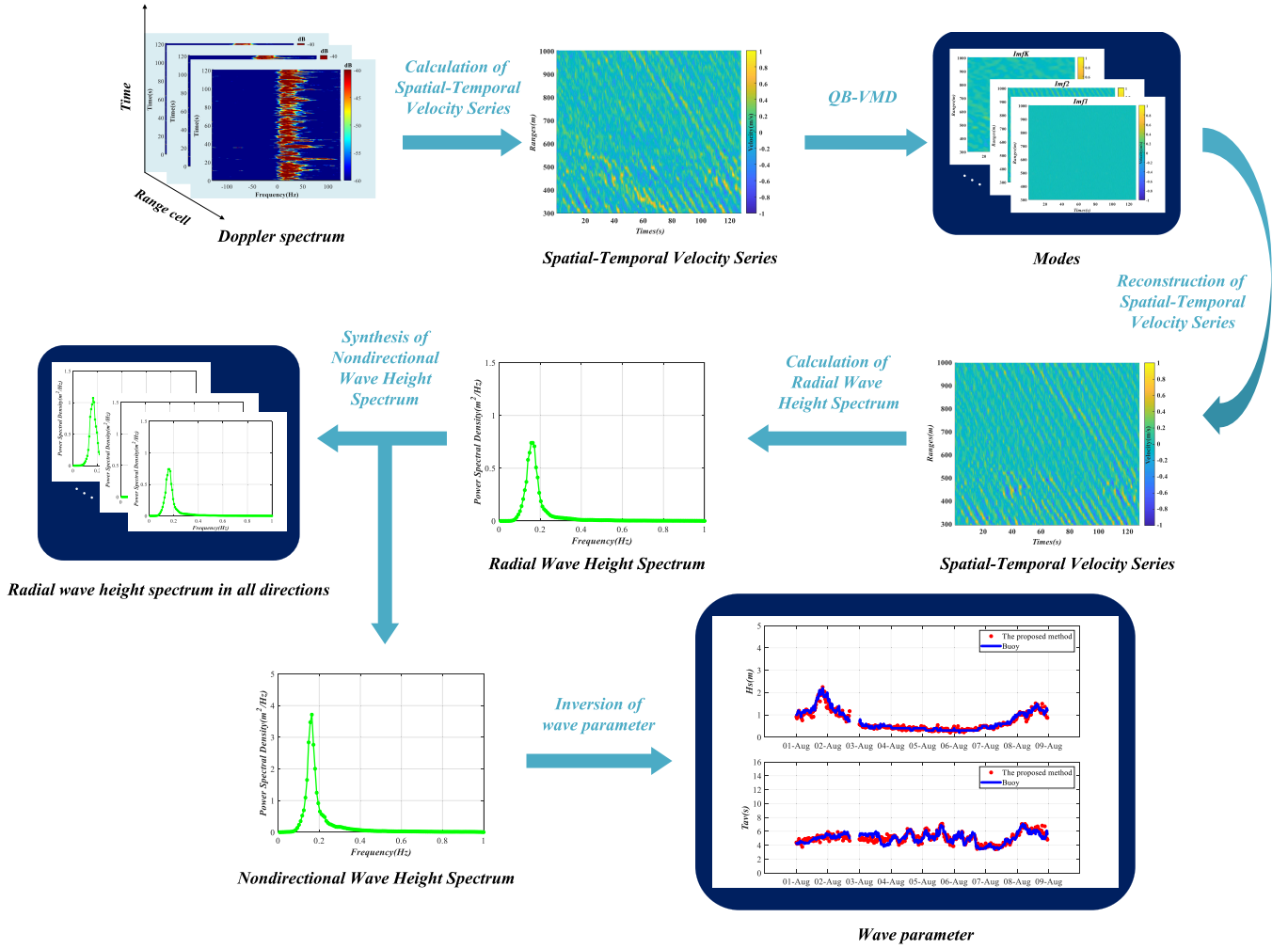
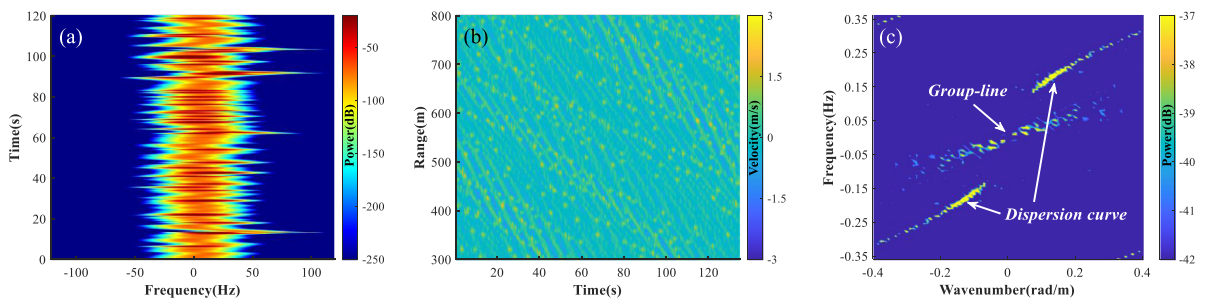Fig. 4. Flowchart of wave parameter inversion.

Fig. 5. Simulated results at the wind speed and fetch of 10 m/s and 80 km, respectively. (a) Time–Doppler spectrum. (b) Spatial–temporal velocity series. (c) Wavenumber–frequency spectrum of (b).

the decomposed length scale along the nonprimary direction (x direction herein) is kept by an additional carrier frequency rebalancing strategy [26]. By QB-VMD, K 2-D IMFs $q_1(x,t), q_2(x,t),...,q_K(x,t)$, with frequencies ranging from high to low are obtained. The 2-D radial velocity and the IMFs satisfy $v_r(x,t) = \sum_{i=1}^{K} q_i(x,t)$. More details on the QB-VMD algorithm can be found in [25] and [31].

According to the optimal theoretical results of the decomposition principle, the sum of the energies of each mode component is equal to the energy of the original spatial–temporal velocity series. When K is too high, fake components will be generated, resulting in energy sum of the components being too high, and vice versa. In order to compensate the deficiency of subjective selection of mode number K, the energy difference is used to
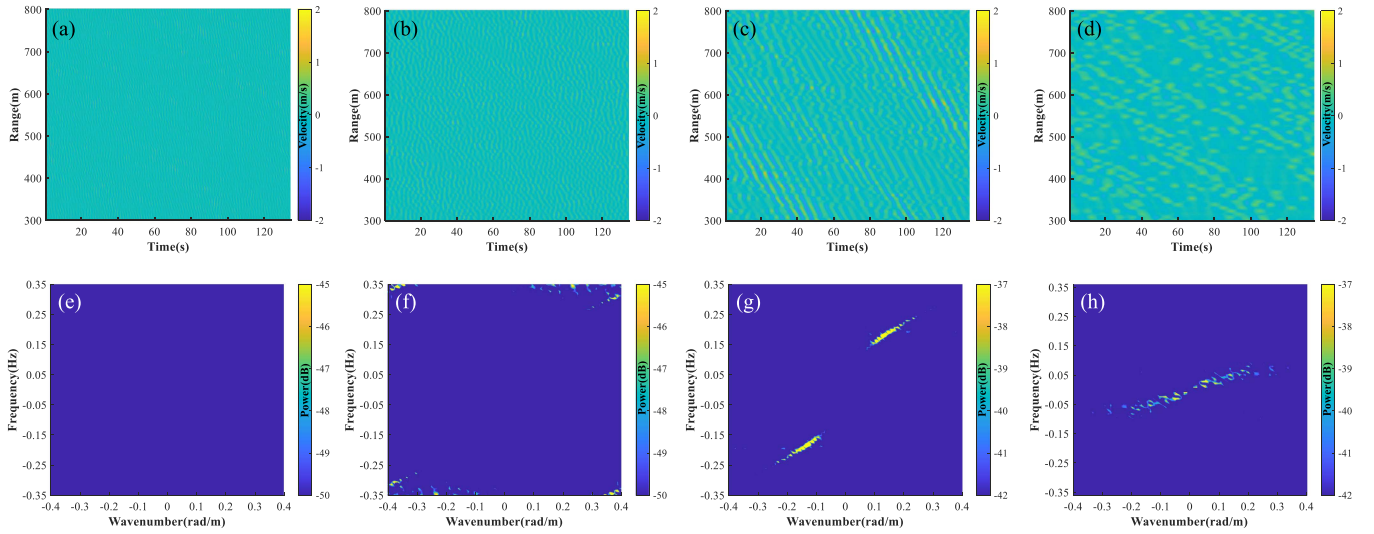
Fig. 6. Each mode and the corresponding wavenumber–frequency spectrum after QB-VMD. (a)–(d) Modes vary from high frequency to low frequency. (e)–(h) Wavenumber–frequency spectrum of (a)–(d).
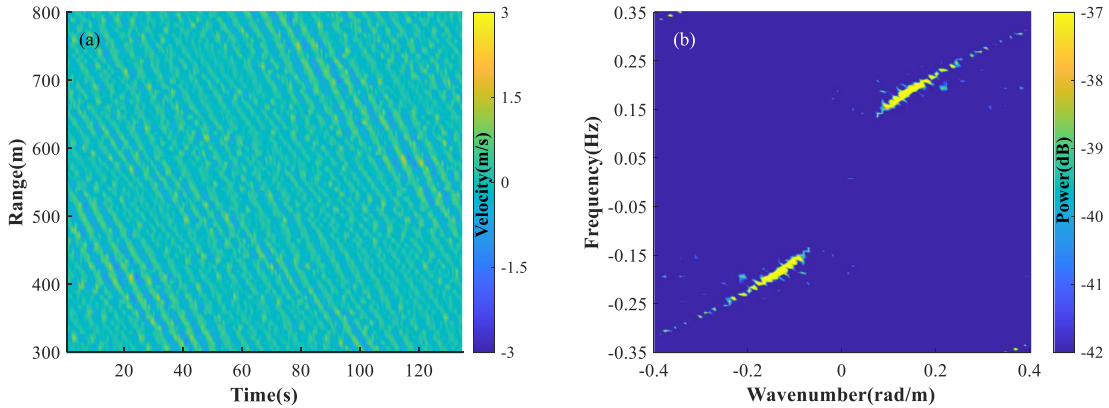

Fig. 7. Reconstructed velocity series and the corresponding wavenumber–frequency spectrum. (a) Reconstructed velocity series. (b) Wavenumber–frequency spectrum of (a).
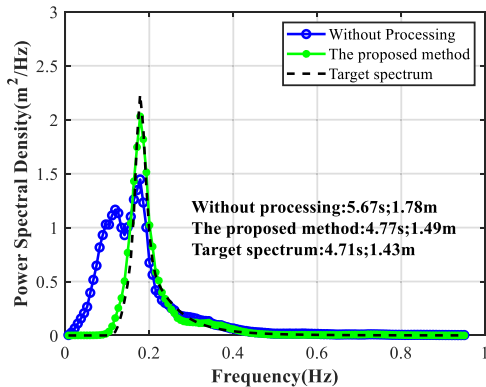

Fig. 8. Comparison of simulated wave height spectrum.

optimize the selection of K value [32]

$$
\begin{cases}
P_{m,l} = \sqrt{\dfrac{\sum_{j=1}^{N}\sum_{i=1}^{M} q_{m,l}^2(k_j,\Omega_i)}{M \cdot N}}, & l = 1,2,\ldots,m \\
P_m = \sum_{l=1}^{m} P_{m,l} \\
\rho_{m,m-1} = \dfrac{|P_m - P_{m-1}|}{P_{m-1}}
\end{cases}
\tag{9}
$$

where M is the time sampling number, N is the range cell number, $q_{m,l}(k,\Omega)$ denotes the lth mode component $q_l(x,t)$ corresponding a 2-D Fourier transform with a decomposed mode number of m, $P_{m,l}$ represents the energy of the lth mode component with a decomposed mode number of m, P_m represents the sum of energy of m modes, and $\rho_{m,m-1}$ is the relative energy difference. For a small m, $v_r(x,t)$ is underdecomposed. When the value of m is too large, $v_r(x,t)$ is overdecomposed. If m increases, the corresponding $\rho_{m,m-1}$ will increase significantly, and $m-1$ will be considered as the optimal number K. Fig. 3(a) shows the measured spatial–temporal velocity series, and Fig. 3(b) shows $\rho_{m,m-1}$ against m of Fig. 3(a). As shown in Fig. 3(b), when $m = 7$, the value of $\rho_{m,m-1}$ is significantly increased, which indicates that the optimal number of modes at this example is $K = 6$.

D. Wave Parameter Inversion Flow

The steps of the QB-VMD method for ocean wave inversion are described, and the flowchart is shown in Fig. 4.

TABLE I
MORSE WAVEFORM PARAMETER

Parameters	Values
Polarization mode	VV
Frequency sweep period	4096 μs
Sampling time	0.5 s
Operating frequency	2.85 GHz
Range resolution	7.5 m

TABLE II
STATISTICAL PARAMETERS (FILTER METHOD/PROPOSED METHOD)

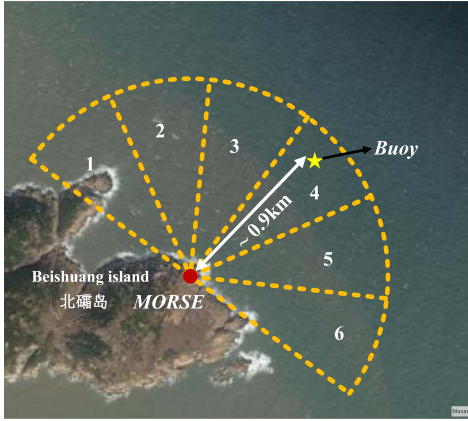|	H_s(m)	T_{av}(s)
MAE	0.14/0.08	0.49/0.37
RMSE	0.19/0.12	0.64/0.49
CC	0.92/0.97	0.69/0.80

Fig. 9. MORSE and buoy position during the experiment.

Step 1 (Calculation of the spatial–temporal velocity series): According to (7), the Doppler frequency shift can be calculated from the radar echo Doppler spectrum, and then, the Doppler velocity can be obtained according to (8). A spatial–temporal velocity series $v_r(x, t, \varphi_n)$ can be obtained, where φ_n is the azimuth angle of the nth antenna. Fig. 3(a) shows a typical spatial–temporal velocity series in which interference stripes and yellow spots can be seen clearly.

Step 2 (QB-VMD): According to the previous section, each slice of the spatial–temporal velocity series is decomposed, and "carrier frequency rebalancing" is performed in the non-decomposition dimension (range dimension) to obtain K 2-D IMFs $q_1(x, t, \varphi_n), q_2(x, t, \varphi_n),...,q_K(x, t, \varphi_n)$, with frequencies ranging from high to low.

Step 3 (Reconstruction of the spatial–temporal velocity series): Broken waves not only generate additional energy at low frequencies in the wave spectrum but also reduce the energy of the dominant waves. Therefore, for reconstructing the spatial–temporal radial velocity series, it is necessary to not only eliminate the low-frequency mode q_K but also compensate for the dominant wave mode q_{K-1} as

$$\hat{v}_r(x, t, \varphi_n) = \sum_{i=1}^{K-1} q_i(x, t, \varphi_n) + \beta \cdot q_{K-1}(x, t, \varphi_n) \quad (10)$$

where $\hat{v}_r(x, t, \varphi_n)$ is the reconstructed spatial–temporal radial velocity series and β is the compensation factor. A smaller β leads to energy loss in the wave spectrum, while a larger β cannot completely eliminate the component of the broken waves. The value of β is validated based on simulated and radar data, and $\beta = 0.8 \cdot E_K/E_{K-1}$ is used in this article, where E_K denote the energy of the Kth mode.

Step 4 (Calculation of the radial wave height spectrum): A wavenumber–frequency spectrum is obtained by the 2-D FFT on the reconstructed spatial–temporal radial velocity series

$$\hat{V}_r(k, f, \varphi_n) = 2\mathrm{DFFT}(\hat{v}_r(x, t, \varphi_n)) \quad (11)$$

and the corresponding velocity power spectrum

$$\hat{V}(k, f, \varphi_n) = |\hat{V}_r(k, f, \varphi_n)|^2. \quad (12)$$

Then, the average velocity spectrum can be estimated as follows [2], [33]:

$$\hat{V}(f, \varphi_n) = \frac{1}{k_{\mathrm{end}} - k_1} \int_{k_1}^{k_{\mathrm{end}}} \hat{V}(k, f, \varphi_n) dk \quad (13)$$

where (k_1, k_{end}) is the wavenumber range. Hence, the radial wave height spectrum of the nth antenna can be obtained

$$\hat{S}(f, \varphi_n) = TF \cdot \hat{V}(f, \varphi_n). \quad (14)$$

Step 5 (Synthesis of nondirectional wave height spectrum): The radial wave height spectrum of the six antennas is superposed to synthesize the nondirectional wave height spectrum as

$$\hat{S}(f) = \sum_n \hat{S}(f, \varphi_n) \cdot \Delta\varphi. \quad (15)$$

Step 6 (Wave parameter inversion): Wave parameters, such as significant wave height and mean wave period, can be obtained from the nondirectional wave height spectrum as follows [34]:

$$H_s = 4\sqrt{m_0} \quad (16)$$

$$T_{\mathrm{av}} = m_0/m_1 \quad (17)$$

where m_0 and m_1 are the zeroth-order and first-order moments of $\hat{S}(f)$, respectively.

III. SIMULATION

According to the Doppler model proposed by Liu et al. [18], the time–Doppler spectra, as well as the spatial–temporal velocity series and wavenumber–frequency spectrum, are simulated as shown in Fig. 5. Similar to Fig. 2(a), "spikes" also appear in Fig. 5(a), indicating an increase in frequency offset at the corresponding location. Correspondingly, the boundary of the sea echoes intermittently widens to the right due to the broken waves. From Fig. 5(b), it can be seen that there are yellow spots in the radial velocity series, which is a broken feature. The "Group-Line" feature in Fig. 5(c) is visible.

To verify the validity of the proposed method, QB-VMD is used to decompose the velocity series in Fig. 5(b), as shown in Fig. 6(a)–(d), representing high-frequency to low-frequency modes. The corresponding wavenumber–frequency spectra are shown in Fig. 6(e)–(h). The figure shows that the first two modes
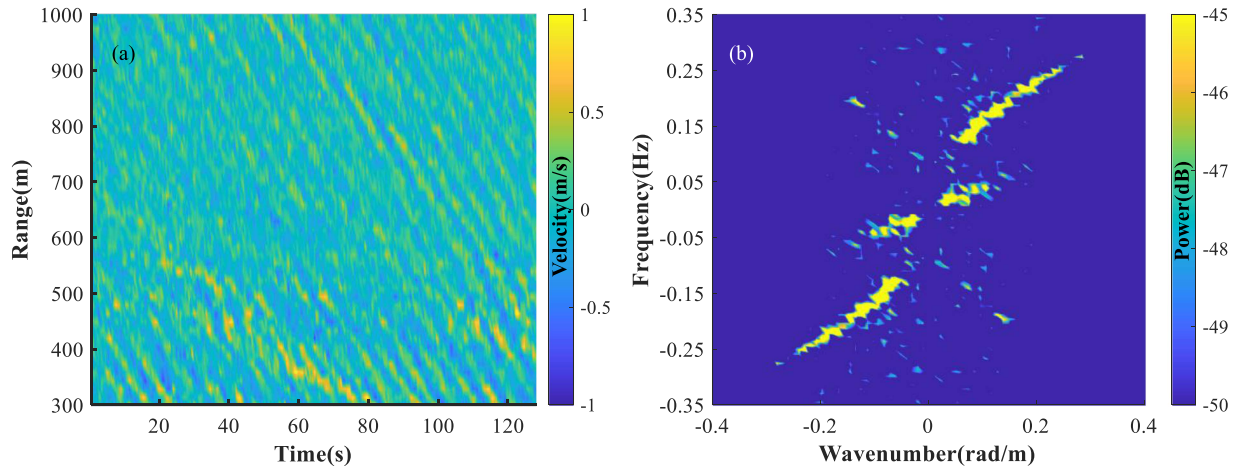
Fig. 10.   Radial velocity series and corresponding wavenumber–frequency spectrum observed by the MORSE on August 8, 2016, at 13:27 with the antenna 3. (a) Radial velocity series. (b) Wavenumber–frequency spectrum of (a).
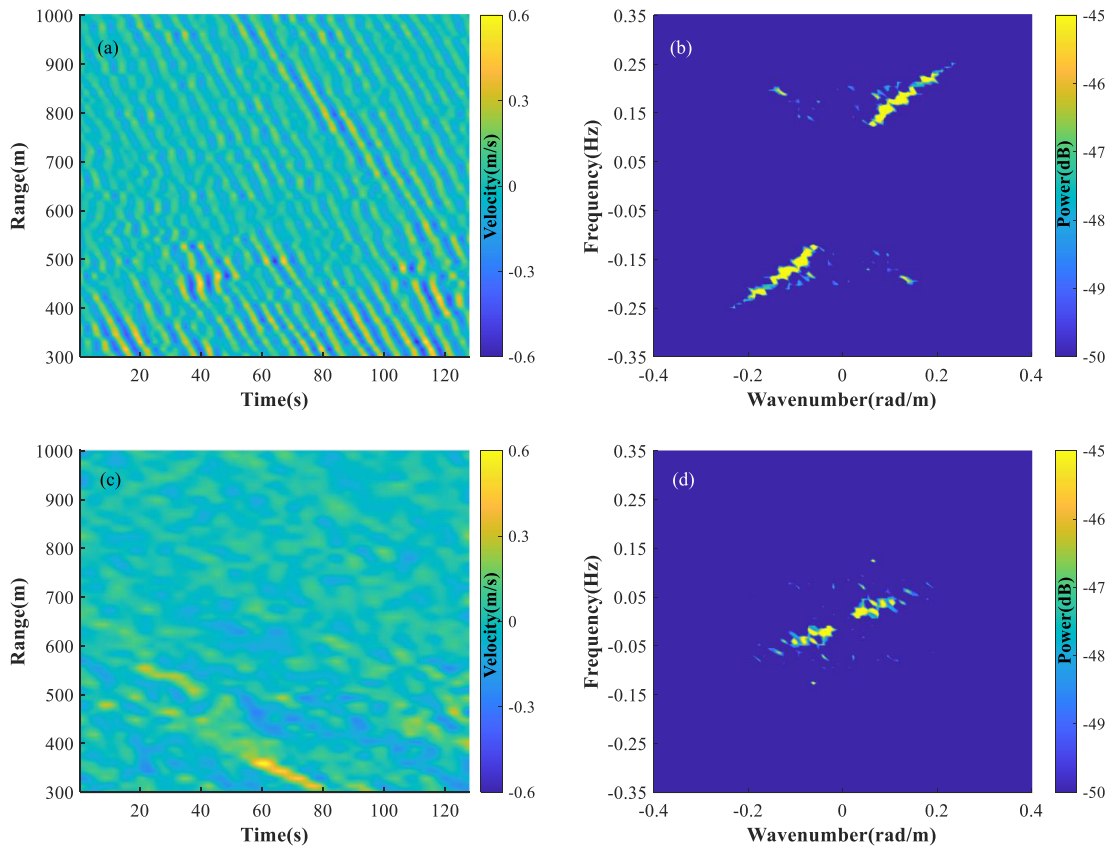

Fig. 11.   QB-VMD. (a) Dominant wave mode. (b) Wavenumber–frequency spectrum of (a). (c) "Group-Line" mode. (d) Wavenumber–frequency spectrum of (c).

are high-frequency modes, and their corresponding energy in the wavenumber–frequency spectrum is relatively low. The third mode is the dominant wave; the interference fringes appear in the velocity series, and the dispersion relation characteristics are presented in the wavenumber–frequency spectrum. The fourth mode is the "Group-Line" mode caused by the broken waves, with low-frequency yellow spots appearing in the velocity series, and its wavenumber–frequency spectrum exhibits a "Group-Line" feature.

The reconstructed velocity series and wavenumber–frequency spectrum are shown in Fig. 7. Comparing Figs. 5 and 7, it can be found that the yellow spots are effectively suppressed in the reconstructed velocity series, the "Group-Line" feature is eliminated in the wavenumber–frequency spectrum, and the energy on the dispersion curve is enhanced.

Fig. 8 shows the estimated wave height spectrum. It can be seen that due to the broken waves, additional low-frequency components are generated in the wave height spectrum, and the
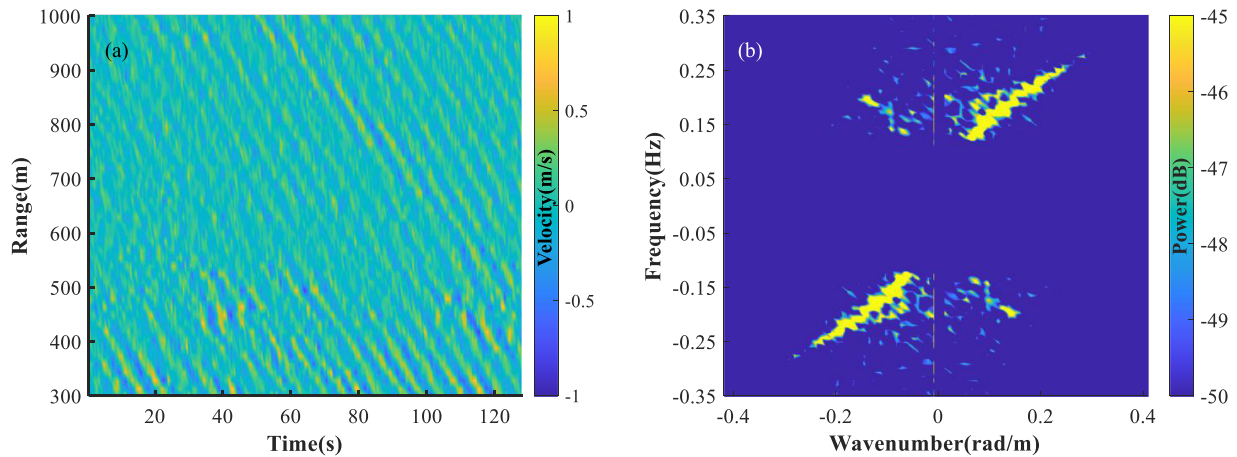
Fig. 12. Reconstructed radial velocity series and corresponding wavenumber–frequency spectrum. (a) Reconstructed radial velocity series. (b) Wavenumber–frequency spectrum of (a).
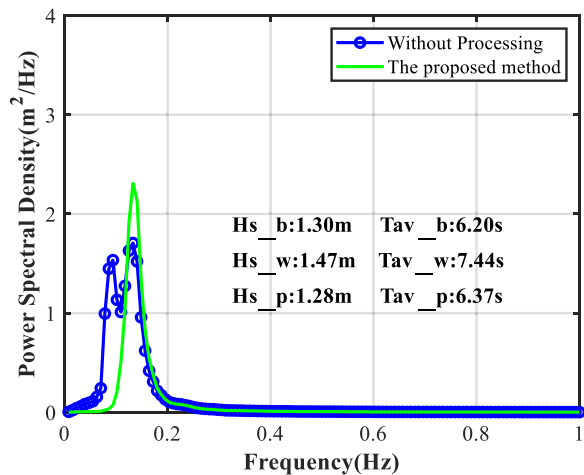

Fig. 13. Comparison of wave height spectra for MORSE observations. The suffixes "b," "w," and "p" represent the observation results of buoys and without processing and the proposed method of MORSE, respectively.

dominant wave energy is reduced. The inverted wave height spectrum using the proposed method not only suppresses the low-frequency components but also compensates for the dominant wave energy, resulting in a more consistent result with the target spectrum.

IV. VERIFIED BY MEASURED DATA

A. Experiment Setup

From August 1 to 8, 2016, an experiment was conducted to evaluate the performance of MORSE wave measurement at Beishuang island, located at northwest of the Taiwan Strait. MORSE adopts a frequency-modulated interrupted continuous wave signal as radio energy transmission and is equipped with six standard horn antennas. Each antenna covers a $30°$ sea surface area and takes 3 min to collect data. The MORSE-related waveform parameters are shown in Table I.

In this experiment, a wave buoy was deployed in the coverage of MORSE as the actual value to verify the radar performance.

The buoy data were lost from 17:00 to 24:00 on August 2. The positions of MORSE and the buoy are shown in Fig. 9. The distance between the MORSE and the buoy is about 0.9 km, and the water depth at the buoy position is about 40 m. During the experiment, the raw radar data at range from 300 to 1000 m is selected in this work and the height of the radar is 50 m, so the incidence angle of the radar in the observation area is $80.5–87.1°$. The buoy provides a measurement every 30 min, and the MORSE measurements are averaged every 30 min for comparison.

B. Verification

Fig. 10 shows the radial velocity series and the corresponding wavenumber–frequency spectrum measured by the antenna 3 at 13:27 on August 8, 2016. The wind speed at that moment was 7.8 m/s and the significant wave height and mean wave period measured by buoy were 1.30 m and 6.20 s, respectively. The wavenumber–frequency spectrum includes "Group-Line" and the dispersion relation curve, consistent with the simulation results in Fig. 5.

Fig. 11 shows the dominant wave mode and the "Group-Line" mode obtained using QB-VMD and the corresponding wavenumber–frequency spectra. In Fig. 11(a), a periodic interference stripe around 5 s appears, while in Fig. 11(c), a large of yellow spots can be seen. Fig. 11(b) and (d) shows the dispersion relation and "Group-Line" distribution, respectively.

The reconstructed spatial–temporal velocity series and the corresponding wavenumber–frequency spectrum are shown in Fig. 12. Compared with Fig. 10(a), the yellow spots in Fig. 12(a) are suppressed, and the interference fringes are enhanced. Accordingly, compared with Fig. 10(b), "Group-Line" energy in the wavenumber–frequency spectrum shown in Fig. 12(b) is filtered out, and the power of the dispersion relation is enhanced.

Fig. 13 shows the nondirectional wave height spectrum synthesized from the measurements of six antennas from 13:12 to 13:30 on August 8, 2016. From Fig. 13, it can be seen that the low-frequency components of the wave height spectrum inverted by the proposed method are suppressed, and the dominant wave
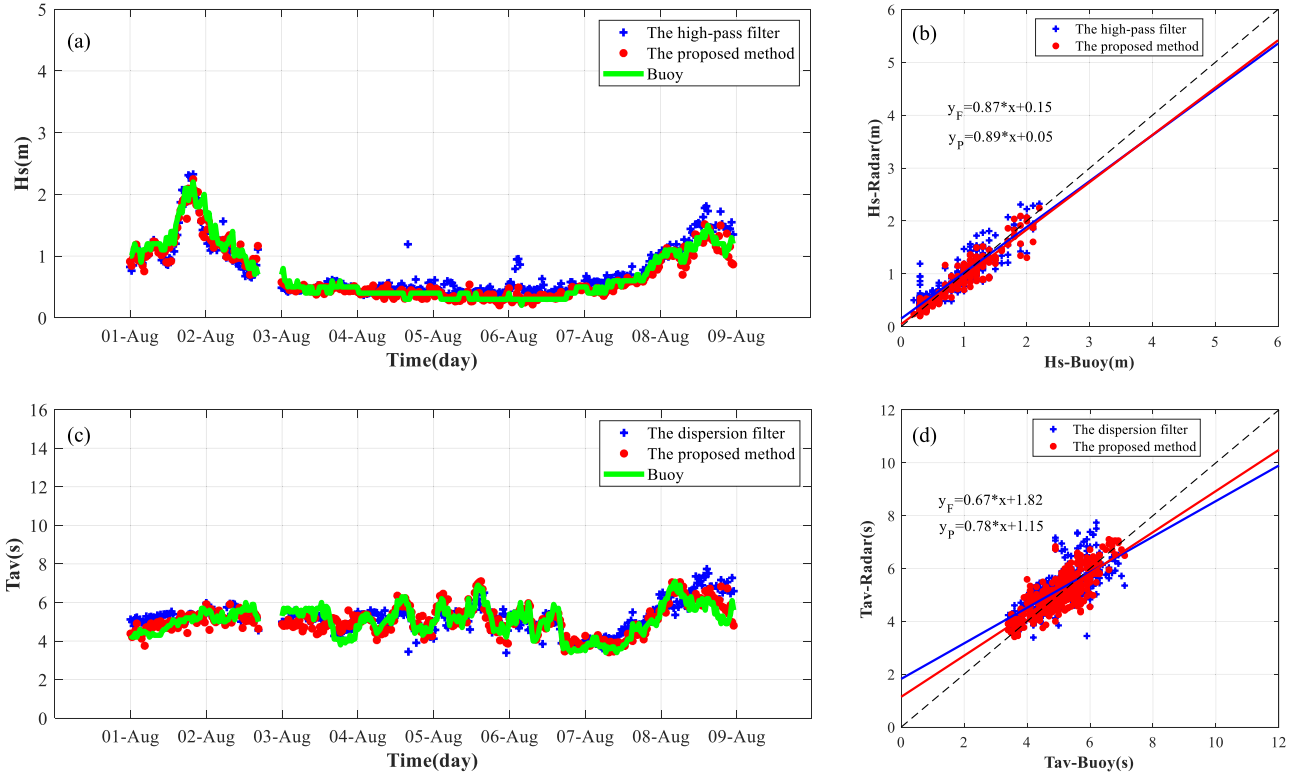
Fig. 14. Comparison of inversion results of ocean wave parameters. (a) Significant wave height series. (b) Scatterplot of significant wave heights. (c) Mean wave period series. (d) Scatterplot of mean wave period.
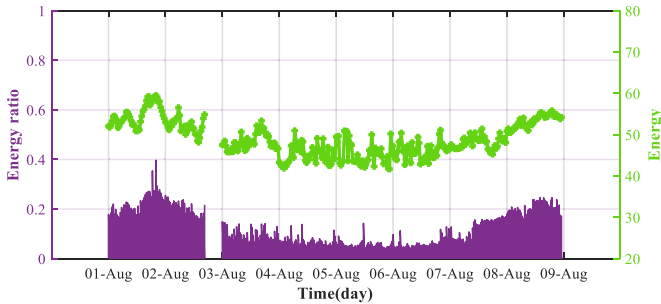

Fig. 15. Time series of energy and energy ratio of the broken wave modes.

component is enhanced. Compared with the buoy observation results, the significant wave height and the mean wave period measured by radar without processing are 1.47 m and 7.44 s, respectively, and the results of the proposed algorithm are 1.28 m and 6.37 s, respectively, which are closer to the buoy observation results (1.30 m and 6.20 s).

C. Results

Eight-day observation data collected with the MORSE are verified by the proposed method. Meanwhile, the inversion methods of significant wave height by a high-pass filter [2] and mean wave period by a dispersion filter [17] are used for comparison. The results of wave parameters retrieved using different methods are shown in Fig. 14. Fig. 14(a) and (c) shows the time series of significant wave height and mean wave period, respectively; the blue plus sign represents the filter

method, the red dot represents the inversion by the proposed method, and the solid green line corresponds to the buoy result. Fig. 14(b) and (d) shows significant wave height and mean wave period scatterplots, respectively. The linear least squares fitting results of the filter method and the proposed method are shown by the solid blue and red lines, respectively, and y_F and y_P represent the corresponding fitting functions, respectively. Table II shows the related statistical parameters: mean absolute error (MAE), root-mean-square error (RMSE), and correlation coefficient (CC).

For the proposed method, MAE, RMSE, and CC of the significant wave height are 0.08 m, 0.12 m, and 0.97, respectively, and the fitting coefficient and bias are 0.89 and 0.05 m, respectively. In comparison, the results of the high-pass filter method are 0.14 m, 0.19 m, and 0.92, respectively, and the fitting coefficient and bias are 0.87 and 0.15 m, respectively. For the proposed method, MAE, RMSE, and CC of the mean wave period are 0.37 s, 0.49 s, and 0.80, respectively, and the fitting coefficient and bias are 0.78 and 1.15 s, respectively. The results of the dispersion filter method are 0.49 s, 0.64 s, and 0.69, respectively, and the fitting coefficient and bias are 0.67 and 1.82 s, respectively. The above results show that the proposed method is more consistent than the filter method. The reason is that the filter method only removes "Group-Line" but fails to compensate for the dominant wave energy. Different from the filter method, the proposed method distinguishes "Group-Line" from the dominant wave and properly compensates for the energy of the dominant wave while removing "Group-Line," which eliminates the influence of the broken wave, and the

retrieved wave parameters are more consistent with the buoy-measured.

Since the proposed method can decompose the broken wave mode from the radial velocity series, the broken wave energy E and the energy ratio E_r can be obtained. It can be expressed by the following equation:

$$E = \iint |\hat{q}_K(k, f)|^2 dk df \qquad (18)$$

$$Er = \frac{E}{\iint \hat{V}(k, f) dk df} \qquad (19)$$

where $\hat{q}_K(k, f)$ denotes the Kth mode component $q_K(x, t)$ (broken wave mode) corresponding a 2-D Fourier transform, and $\hat{V}(k, f)$ is the velocity power spectrum of the reconstructed spatial–temporal velocity series. The time series of energy and energy ratio of the broken wave modes are shown in Fig. 15. During the experiment, the broken wave energy is consistent with the trend of the significant wave height with a CC of 0.87, which indicates that the broken wave energy is related to the sea state. The broken wave energy is higher under the high sea state (August 1, 2, and 8) than under the low sea state (August 3–7). Another interesting phenomenon is that the ratio of the broken wave energy to the total energy is also dependent on the sea state, and the CC between the energy ratio and the significant wave height is 0.96. The energy ratio is greater than 0.15 under the high sea state and around 0.1 under the low sea state. The reason for these two phenomena is that when the sea state is high, the sea surface wave displacement slope becomes steep enough, and it is easier to satisfy the broken wave generation conditions. On the contrary, under the low sea state, the slope of the sea surface wave surface displacement is difficult to reach the broken wave generation condition, so the broken wave energy is smaller and the energy ratio is smaller under the low sea state.

V. Conclusion

In this article, a new method for wave parameter inversion based on the QB-VMD algorithm has been proposed. First, QB-VMD is used to decompose the spatial–temporal radial velocity series to obtain a series of modes. Then, the "Group-Line" mode is removed, and the dominant wave mode is compensated appropriately to get the reconstructed spatial–temporal radial velocity series. Finally, the parameters of ocean waves are retrieved according to the reconstructed spatial–temporal radial velocity series. The simulation results show that the proposed method can suppress the low-frequency component of the wave height spectrum caused by the broken wave and compensate for the dominant wave component. In addition, the eight-day dataset collected by MORSE deployed in Beishuang island is used to invert the wave parameters. The results have shown that the proposed method can retrieve the wave parameters with a reasonable performance. In the future, the correctness of the method needs to be verified under more different sea states.

References

[1] R. Bouchard, K. Steele, C. Teng, L. Fiorentino, and T. Rutledge, "Some theory and application of calibration techniques for NDBC wave measurement buoys," in *Proc. Regional Mar. Instrum. Centre WMO Region Workshop*, 2016, pp. 14–15.

[2] Z. Chen, H. Liu, C. Zhao, and C. Zhang, "Spatial-temporal inversion algorithm for wave measurements using shore-based coherent S-band radar," *IEEE Trans. Geosci. Remote Sens.*, vol. 60, 2022, Art. no. 5102914.

[3] Z. Chen, X. Chen, C. Zhao, J. Li, W. Huang, and E. W. Gill, "Observation and intercomparison of wave motion and wave measurement using shore-based coherent microwave radar and HF radar," *IEEE Trans. Geosci. Remote Sens.*, vol. 57, no. 10, pp. 7594–7605, Oct. 2019.

[4] X. Chen, W. Huang, C. Zhao, and Y. Tian, "Rain detection from X-band marine radar images: A support vector machine-based approach," *IEEE Trans. Geosci. Remote Sens.*, vol. 58, no. 3, pp. 2115–2123, Mar. 2020.

[5] X. Chen and W. Huang, "Spatial–temporal convolutional gated recurrent unit network for significant wave height estimation from shipborne marine radar data," *IEEE Trans. Geosci. Remote Sens.*, vol. 60, 2022, Art. no. 4201711.

[6] W. J. Plant and W. C. Keller, "Evidence of Bragg scattering in microwave Doppler spectra of sea return," *J. Geophys. Res.: Oceans*, vol. 95, no. C9, pp. 16299–16310, 1990.

[7] Z. Chen, L. Fan, C. Zhao, and Y. Jin, "Ocean wave directional spectrum measurement using microwave coherent radar with six antennas," *IEICE Electron. Exp.*, vol. 9, no. 19, pp. 1542–1549, 2012.

[8] Z. Chen, Z. Wang, X. Chen, C. Zhao, F. Xie, and C. He, "S-band Doppler wave radar system," *Remote Sens.*, vol. 9, no. 12, 2017, Art. no. 1302.

[9] E. E. Hackett, A. M. Fullerton, C. F. Merrill, and T. C. Fu, "Comparison of incoherent and coherent wave field measurements using dual-polarized pulse-Doppler X-band radar," *IEEE Trans. Geosci. Remote Sens.*, vol. 53, no. 11, pp. 5926–5942, Nov. 2015.

[10] W. Plant, W. Keller, and K. Hayes, "Measurement of river surface currents with coherent microwave systems," *IEEE Trans. Geosci. Remote Sens.*, vol. 43, no. 6, pp. 1242–1257, Jun. 2005.

[11] H. Chien, H. Y. Cheng, and D. B. Trizna, "Determination of phase difference of backscatter signals from coherent-on-receive microwave marine radar for wave measurement," in *Proc. OCEANS Conf.*, 2013, pp. 1–6.

[12] J. He, Z. Chen, C. Zhao, X. Chen, Y. Wei, and C. Zhang, "Wave parameter inversion with coherent microwave radar using spectral proper orthogonal decomposition," *IEEE Trans. Geosci. Remote Sens.*, vol. 60, 2022, Art. no. 2006311.

[13] C. Zhao, X. Wang, Z. Chen, S. Wu, and Y. Zeng, "Inversion of wave parameters from time-Doppler spectrum using shore-based coherent S-band radar," *IEEE Trans. Geosci. Remote Sens.*, vol. 61, 2023, Art. no. 5101211.

[14] W. J. Plant, "Microwave sea return at moderate to high incidence angles," *Waves Random Media*, vol. 13, no. 4, pp. 339–354, 2003.

[15] C. Stevens, E. Poulter, M. Smith, and J. McGregor, "Nonlinear features in wave-resolving microwave radar observations of ocean waves," *IEEE J. Ocean. Eng.*, vol. 24, no. 4, pp. 470–480, Apr. 1999.

[16] W. J. Plant and G. Farquharson, "Origins of features in wave number-frequency spectra of space-time images of the ocean," *J. Geophys. Res.: Oceans*, vol. 117, no. C6, pp. 1–10, Jun. 2012.

[17] H. Liu, Z. Chen, C. Zhao, and S. Wu, "Improvement of mean wave period based on dispersion relation filter using shore-based coherent s-band radar," *J. Atmos. Ocean. Technol.*, vol. 39, no. 8, pp. 1105–1113, 2022.

[18] H. Liu, Z. Chen, and C. Zhao, "A new Doppler model incorporated with free and broken-short waves for coherent S-band wave radar at near-grazing angles," *IEEE Trans. Geosci. Remote Sens.*, vol. 60, 2022, Art. no. 5108311.

[19] A. J. Kammerer and E. E. Hackett, "Group line energy in phase-resolved ocean surface wave orbital velocity reconstructions from X-band Doppler radar measurements of the sea surface," *Remote Sens.*, vol. 11, no. 1, 2019, Art. no. 71.

[20] A. J. Kammerer, "The application of proper orthogonal decomposition to numerically modeled and measured ocean surface wave fields remotely sensed by radar," Ph.D. dissertation, Dept. Coastal Marine Syst. Sci., Coastal Carolina Univ., Conway, SC, USA, 2017.

[21] A. J. Kammerer and E. E. Hackett, "Use of proper orthogonal decomposition for extraction of ocean surface wave fields from X-band radar measurements of the sea surface," *Remote Sens.*, vol. 9, no. 9, 2017, Art. no. 881.

[22] P. A. Hwang, M. A. Sletten, and J. V. Toporkov, "A note on Doppler processing of coherent radar backscatter from the water surface: With application to ocean surface wave measurements," *J. Geophys. Res.: Oceans*, vol. 115, no. C3, 2010.

[23] R. Carrasco, J. Horstmann, and J. Seemann, "Significant wave height measured by coherent X-band radar," *IEEE Trans. Geosci. Remote Sens.*, vol. 55, no. 9, pp. 5355–5365, Sep. 2017.

[24] Z. Yang and W. Huang, "Wave height estimation from X-band radar data using variational mode decomposition," *IEEE Geosci. Remote Sens. Lett.*, vol. 19, 2022, Art. no. 1505405.

[25] W. Wang, C. Pan, and J. Wang, "Quasi-bivariate variational mode decomposition as a tool of scale analysis in wall-bounded turbulence," *Experiments Fluids*, vol. 59, no. 1, p. 1, 2018.

[26] C. Pan and Y. Kwon, "Extremely high wall-shear stress events in a turbulent boundary layer," *J. Phys. Conf. Ser.*, vol. 1001, 2018, Art. no. 012004.

[27] W. J. Plant, W. C. Keller, and J. W. Wright, "Modulation of coherent microwave backscatter by shoaling waves," *J. Geophys. Res.: Oceans*, vol. 83, no. C3, pp. 1347–1352, 1978.

[28] W. J. Plant, "A model for microwave Doppler sea return at high incidence angles: Bragg scattering from bound, tilted waves," *J. Geophys. Res.: Oceans*, vol. 102, no. C9, pp. 21131–21146, 1997.

[29] W. Plant, "Bound waves and sea-surface slopes," in *Proc. Oceans Conf.*, 2003, vol. 4, pp. 1825–1828.

[30] W. J. Plant, W. C. Keller, V. Hesany, T. Hara, E. Bock, and M. A. Donelan, "Bound waves and Bragg scattering in a wind-wave tank," *J. Geophys. Res.: Oceans*, vol. 104, no. C2, pp. 3243–3263, 1999.

[31] K. Dragomiretskiy and D. Zosso, "Variational mode decomposition," *IEEE Trans. Signal Process.*, vol. 62, no. 3, pp. 531–544, Mar. 2014.

[32] Y. Zhang, R. Li, and J. Zhang, "Optimization scheme of wind energy prediction based on artificial intelligence," *Environ. Sci. Pollut. Res.*, vol. 28, pp. 39966–39981, 2021.

[33] R. M. Sorensen, *Basic Wave Mechanics: For Coastal and Ocean Engineers*. Hoboken, NJ, USA: Wiley, 1993.

[34] Y. Goda, *Random Seas and Design of Maritime Structures*, vol. 33. Singapore: World Scientific, 2010.

Zezong Chen received the B.S. and M.Eng. degrees in electronic engineering in 1987 and 1993, respectively, and the Ph.D. degree in radio physics in 2005, all from Wuhan University, Wuhan, China.

Since 1993, he has been with the School of Electronic Information, Wuhan University, where he is currently a Professor carrying out teaching and research in electronic engineering. His research interests include radar systems and theory, and application of high-frequency and microwave radar in remote sensing of the marine environment.

Chen Zhao (Member, IEEE) received the B.S. degree in communication engineering and the Ph.D. degree in radio physics from Wuhan University, Wuhan, China, in 2007 and 2012, respectively.

In 2012, he was a Postdoctoral Researcher in radio physics with Wuhan University. From 2018 to 2019, he was a Visiting Scholar with the Memorial University of Newfoundland, St. John's, NL, Canada. Since 2015, he has been with the School of Electronic Information, Wuhan University, where he is currently an Associate Professor carrying out teaching and research in electronic engineering. He is also a Joint Professor with the Donghai Laboratory, Zhoushan, China. His research interests include application of high-frequency and microwave radar in remote sensing of the marine environment.

Dr. Zhao is an Associate Editor for IEEE CANADIAN JOURNAL OF ELECTRICAL AND COMPUTER ENGINEERING and *Chinese Journal of Ship Research*.

Zhongqian Hu received the B.E. degree in information management and information system from the Anhui University of Technology, Ma'anshan, China, in 2018. He is currently working toward the Ph.D. degree in electronic information with Wuhan University, Wuhan, China, supervised by Prof. Zezong Chen.

His research interests include signal processing and ocean remote sensing based on microwave radar.

Xi Chen received the B.S. degree in electronic engineering and the Ph.D. degree in circuits and systems from Wuhan University, Wuhan, China, in 2014 and 2020, respectively.

He is currently with the China Ship Development and Design Center, Wuhan. His research interests include radar systems and ship motion prediction.